

# Optimum Particle Size in Silicon Electrodes Dictated by Chemomechanical Deformation of the SEI

Mok Yun Jin, Kai Guo, Xingcheng Xiao, Mark W. Verbrugge, Huajian Gao, and Brian W. Sheldon\*

Nanostructured alloy-forming anode materials can resist fracture that is caused by extreme volume changes during cycling. However, the higher surface area per unit mass in nanomaterials increases exposure to the electrolyte reduction reactions that form a solid electrolyte interphase (SEI), which implies that capacity loss will increase as particle size decreases. This hypothesis is investigated with composite electrodes using different silicon nanoparticle sizes, and the expected particle size effect is not observed. Instead, there is an optimum particle size where capacity loss per volume is minimized. Finite element modeling demonstrates that the mechanical deformation of the SEI varies significantly with the silicon particle size. Smaller particles lead to the decrease of the tensile hoop strains in the outer portion of the SEI and simultaneously make the overall elastic strains in the inner portion more compressive. These results suggest that the SEI on smaller particles is more resistant to mechanical degradation, even though the higher specific surface areas increase initial SEI formation. The trade-off between these effects leads to the observed optimum particle size.

## 1. Introduction

There is currently a major global effort to create rechargeable batteries with improved energy density and safety to enable

M. Y. Jin, Dr. K. Guo, Prof. H. Gao, Prof. B. W. Sheldon  
School of Engineering  
Brown University  
Providence, RI 02912, USA  
E-mail: brian\_sheldon@brown.edu

Dr. K. Guo  
Department of Civil and Environmental Engineering  
Massachusetts Institute of Technology  
Cambridge, MA 02139, USA

Dr. X. Xiao, Dr. M. W. Verbrugge  
Chemical and Materials Systems Laboratory  
General Motors Research and Development Center  
Warren, MI 48090, USA

Prof. H. Gao  
School of Mechanical and Aerospace Engineering  
College of Engineering  
Nanyang Technological University  
Singapore 637457, Singapore

Prof. H. Gao  
Institute of High Performance Computing  
A\*STAR  
Singapore 138632, Singapore

 The ORCID identification number(s) for the author(s) of this article can be found under <https://doi.org/10.1002/adfm.202010640>.

DOI: 10.1002/adfm.202010640

advanced devices, such as electric vehicles. This requires crucial innovations in battery materials. Alloy-forming materials with Li such as Si, Ge, and Sn are considered promising negative electrodes with much greater theoretical capacity than state-of-the-art graphite electrodes.<sup>[1,2]</sup> However, the large number of Li atoms inserted into these alloy anode materials lead to extreme volume changes.<sup>[3]</sup> Such expansion/contraction during lithiation/delithiation can lead to substantial structural changes inside of electrodes, which in turn are believed to cause substantial capacity decay due to chemomechanical phenomena.<sup>[4,5]</sup> In particular the solid electrolyte interphase (SEI) layer which passivates electrode surfaces must retain its integrity, while the underlying active material undergoes severe structural changes during electrochemical cycling.<sup>[6–9]</sup> The

coupled mechanical and chemical degradation of the SEI is widely proposed as a primary factor that limits cycle life of Si-containing electrodes (noted for their high theoretical capacity of  $\approx 4200 \text{ mAh g}^{-1}$ ).<sup>[10–12]</sup> However, mechanical deformation and degradation of the SEI in the electrochemical environment are extremely difficult to investigate due to the complex microstructure of electrodes.

Nanostructured silicon materials such as thin-films, nanowires, and nanoparticles can resist fracture during lithiation and delithiation.<sup>[13,14]</sup> However, the higher specific surface area in these nanomaterials increases exposure to electrolyte reduction reactions. This is widely believed to induce more irreversible lithium loss, however, this direct correlation with initial surface area neglects the impact that size effects have on the strain tolerance of the SEI.<sup>[15,16]</sup> To obtain insight into this phenomenon, a systematic investigation was conducted with Si nanoparticle composite electrodes. A continuum analysis based on finite element modeling (FEM) was then employed to analyze the impact of particle size on the mechanical deformation of the SEI. Detailed results from these investigations provide direct and quantitative information about the strain-induced capacity loss in silicon particle-based electrodes. The impact of silicon particle size on the SEI mechanical stability has not been systematically documented in prior work, and the current study demonstrates that the capacity losses are not simply proportional to the initial surface area of the electrodes. The particle size has two opposing effects on Si-based electrodes: smaller

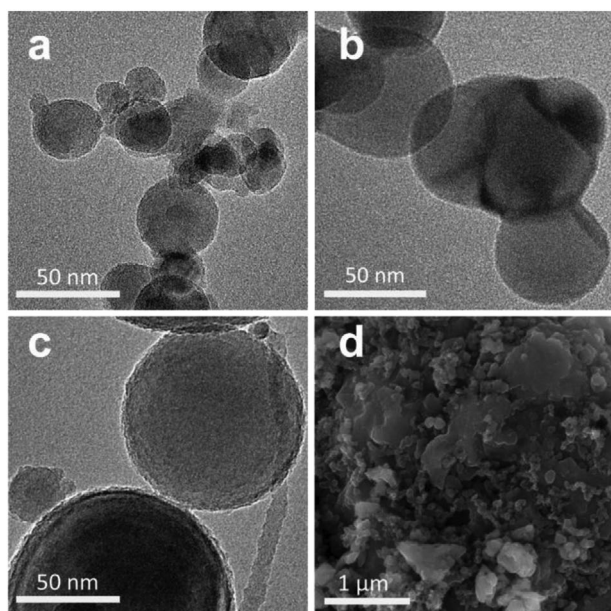


**Figure 1.** HR-TEM images of the Si NPs: a) 30 nm, b) 80 nm, c) 100 nm. d) SEM image of as-made composite electrodes using 500 nm Si NPs.

particles lead to more chemical degradation due to the higher surface area, but less mechanical degradation due to more stabilized SEI and Si. The optimum particle size observed here is unexpected. This work, along with the corresponding analysis, provides new insight about the implementation of nanostructured high-capacity alloy anode materials that are subjected to large volume changes during cycling.

## 2. Results and Discussion

### 2.1. Electrochemical Cycling of Silicon Nanoparticles

Four types of samples with different Si NP sizes ( $D = 30, 80, 100,$  and  $500$  nm) were investigated (5–7 electrodes of each type). **Figure 1** shows the high-resolution transmission electron microscopy (HR-TEM) images of different Si NP sizes and the scanning electron microscope (SEM) image of the as-made composite electrodes using 500 nm Si NPs. While the 30, 80, and 100 nm samples are spherical, the 500 nm particles

are more randomly shaped. Particle size distributions were obtained for each powder sample (30, 80, and 100 nm) using TEM images ( $>130$  particles) and the statistic results confirm that the size distributions were relatively uniform as seen in Figure S1 (Supporting Information). It is worth noting that the electrodes were prepared by varying only the Si NP sizes with everything else fixed. Every composite electrode sample was prepared to contain Si NP/CB/CMC in weight ratios of 70/15/15.

The electrochemical cycling conditions were designed to explore the impact of particle size on capacity losses. These were based on recent work by Zhang et al., where a novel in situ method was used to investigate relationships between the SEI formation conditions and capacity loss of silicon thin film samples.<sup>[12]</sup> This work quantitatively shows that the large strain-induced capacity losses are induced by the applied tensile strain in the SEI during lithiation. With this in mind, the aforementioned method was adopted to evaluate the impact of particle size on strains in the SEI and capacity loss.

It is generally believed that the SEI is formed primarily during the first cycle, such that different cycling conditions during the first cycle create different initial SEI structures.<sup>[14,17]</sup> Initial SEI's were created for each type of Si NP-based composite electrodes at C/20 to 0.05 V and C/20 from 0.05 to 1.5 V as shown in **Figure 2a**. At the end of each delithiation process, the voltage was held at 1.5 V for 5 h to ensure complete lithium removal. For each of these conditions, a total of 20 samples were tested (5 each of 4 different samples). After the SEI formation cycle as described above, three sequences followed each consisting of seven symmetric galvanostatic discharge–charge steps run at C/20. The cut-off voltages for these steps progressively went down lower (0.6, 0.5, 0.4, 0.3, 0.2, 0.1, 0.05 V) as shown in **Figure 2b**. The capacity loss measured during such symmetric lithiation–delithiation cycles to each of these voltages provides a direct measure of lithium that is not recovered over this range. A subsequent cycle to a lower voltage provides information of the additional SEI losses for the additional increment. The full sequence then provides a set of capacity loss values, which reflects SEI formation over the different voltage ranges. Each sequence is designed to provide insight into the dynamic behavior of strains in the SEI layer.

In comparison with the work previously reported by Zhang et al., an additional full set of cycles (sequence 3) were employed with the particle-based composite electrodes. Another

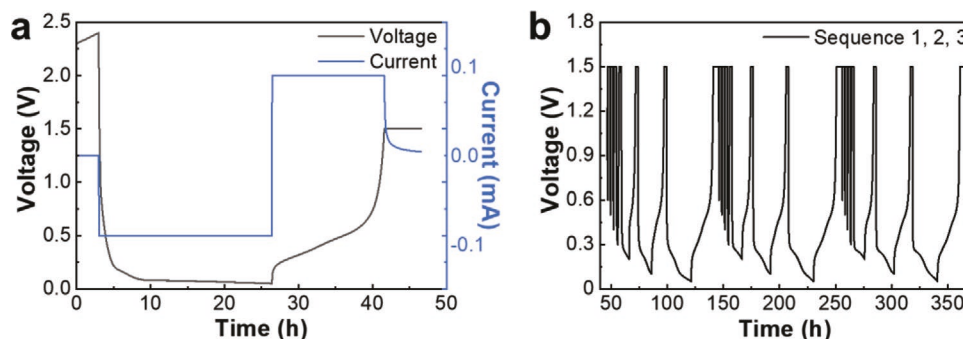


**Figure 2.** a) Slow formation cycle (C/20) described in the text is shown here. b) Sequences of seven galvanostatic cycles were used to monitor capacity loss at different SOC.

**Table 1.** Capacities of Si nanoparticles during the formation (first) cycle and at the end of sequence 1. Measured oxide thickness of the 30, 80, and 100 nm particles from TEM and the estimated capacity reduction due to the oxide shell.

Samples [nm]	Formation		End of Sequence 1	Oxide layer thickness [nm]	Estimated capacity reduction by oxide shell [mAh g <sup>-1</sup> ]
	Lithiation capacity	Delithiation capacity	Delithiation capacity		
	[mAh g <sup>-1</sup> ]				
30	2375 ± 87	1726 ± 22	2246 ± 98	2 ± 0.5	1242 ± 270
80	2960 ± 75	2612 ± 77	3077 ± 199	1 ± 0.5	261 ± 128
100	3256 ± 19	3051 ± 21	3309 ± 86	1 ± 0.5	210 ± 146
500	3169 ± 27	2971 ± 32	2462 ± 253	–	–

important difference between these studies is that the Si NPs are initially crystalline, such that an amorphous to crystalline phase transformation occurs during cycling. This was evaluated with X-ray diffraction measurements after the SEI formation cycle and the subsequent cycles.

## 2.2. Capacity Measurements

Measured capacities during the formation cycle and at the end of sequence 1 are shown in **Table 1** and the representative initial charge–discharge curves of the four samples are provided in Figure S1 (Supporting Information). The capacity losses during the formation cycle are primarily due to SEI formation. It can be seen that irreversible capacities in the formation cycle increase as particle size decreases partly due to increase of specific surface areas for SEI formation. The relatively low capacities of the 30 nm are attributed to a thicker oxide layer (see Figure S2, Supporting Information). Measured oxide thicknesses from TEM in Figure S1b–d (Supporting Information) indicate that these native oxides reduce the available Si for lithiation by around 22% for 30 nm particles. X-ray diffraction (Figure S3, Supporting Information) confirms that most of the crystalline Si is converted to amorphous Si during Sequence 1, even for the largest particle size ( $D = 500$  nm).

As mentioned above, the electrochemical cycling conditions are designed such that the silicon lithiation states are controlled by different cut-off voltages. After sequence 2, the delithiation capacity of the 80 nm particles increases to 3309 mAh g<sup>-1</sup>, which is close to the maximum lithium capacity in silicon (see Figure S4, Supporting Information). The slight increase of the capacities with cycling after the formation cycle is probably due to further contact and activation of the particles.<sup>[13,18–20]</sup> In contrast to this, capacities of the larger particles (i.e., 500 nm) fade substantially from sequence to sequence.

The measured capacity loss for each cycle is given by

$$\Delta c = \frac{C^{\text{lith}} - C^{\text{delith}}}{m_{\text{si}}} \quad (1)$$

where  $m_{\text{si}}$  is the mass of Si in the electrode and  $C^{\text{lith}}$  and  $C^{\text{delith}}$  are measured capacities during the lithiation and delithiation steps, respectively. Because SEI formation is associated with surfaces, one might expect to see losses that scale with the particle surface area. To assess this, the capacities were normalized to obtain specific losses per area via

$$\Delta \hat{c} = \frac{\rho \Delta c}{S_v} \quad (2)$$

where  $S_v$  is the specific surface area of an un lithiated particle and  $\rho$  is the Si density. Assuming all particles are perfectly spherical with radius  $r_{\text{si}}$ , the initial specific surface area of a particle can be obtained based on the following

$$S_v = \frac{4\pi R_o^2}{\frac{4}{3}\pi R_o^3} = \frac{3}{R_o} \text{ (cm}^{-1}\text{)} \quad (3)$$

The average value of  $R_o$  provided by the vendor was used for all estimates. Microscopy showed size variations for each sample, but these distributions were relatively narrow.

**Figure 3** reports specific capacity losses for samples with different Si particle sizes (30, 80, 100, and 500 nm). For cycles run to 0.6, 0.5, and 0.4 V, the samples have relatively small capacities due to limited silicon lithiation (see Figure S4, Supporting Information). Capacity losses increase substantially at lower

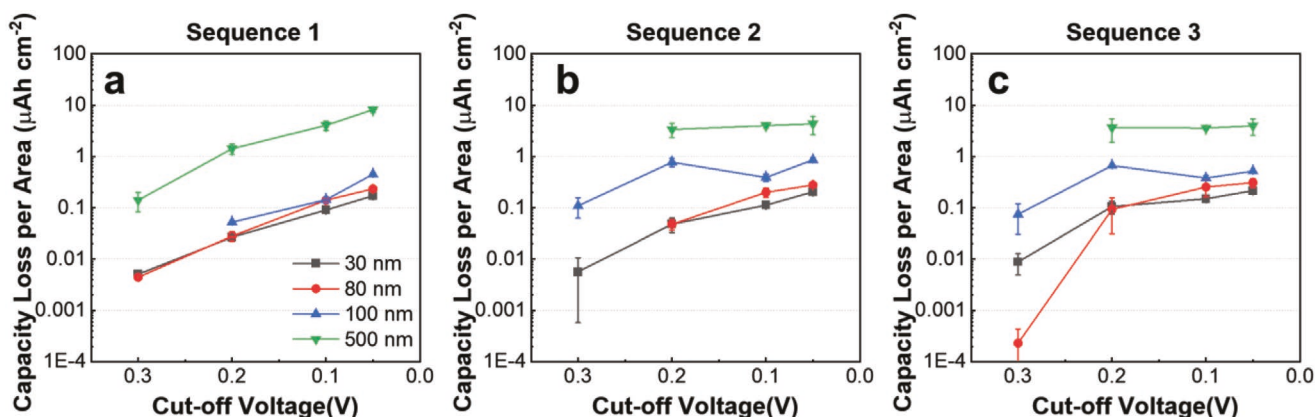


**Figure 3.** Log plots of irreversible capacities of Si NPs: a) sequence 1; b) sequence 2; and c) sequence 3.

potentials, where further lithiation of the silicon leads to larger strains. The results in Figure 3 show that the losses at a given potential vary substantially with particle size. These are the primary data that are used for our analysis of SEI degradation.

The large increase in specific capacity loss with increasing particle size is an important finding. Prior work with carbon electrodes shows that capacity loss due to SEI formation is proportional to the specific surface area.<sup>[15]</sup> This is often used to argue that nanosized electrode materials lead to high capacity losses.<sup>[16,21–26]</sup> However, our results indicate that the situation with silicon electrodes is more complex. The comparison between the 30 and 80 nm data in this study provides the strongest basis for a quantitative comparison, because these powders (obtained from the same vendor) were produced with the same synthesis methods. The 500 nm particles have a very different morphology and wider distribution of sizes as shown in Figure 1d. Despite these differences, the experiments clearly show that specific capacity loss per surface area increases with the particle size.

It has been proposed that fracture is more likely to occur in larger particles during cycling, and this could have an impact on the measured capacity losses.<sup>[27]</sup> Liu et al. predict that fracture should occur during the first lithiation if the diameter is above 150 nm.<sup>[28]</sup> SEM images (Figure S5, Supporting Information) show that the size of the 500 nm particles increases after the formation cycle (consistent with other work showing net volume expansion after delithiation of silicon). This suggests that even if the 500 nm particles fracture, their effective particle size is still much larger than the smaller particles that were investigated. Based on this, fracture of the 500 nm particles does not appear to cause enough increase in surface area to account for the much higher specific capacity losses in Figure 3.

The comparisons in Figure 3 are based on the premise that SEI-related losses are largely related to the available surface area, whereas capacity and particle expansion/contraction are volumetric effects. During cycling it is important to note that the larger relative surface area of smaller particles will lead to lower current density than the larger particles at the same C-rate. It is possible that this difference has an impact on the lower capacity losses observed with the smaller particles. Several prior investigations with anode materials (primarily graphite) have related formation current densities to the SEI composition and structure in particle-based electrodes.<sup>[29–33]</sup> These studies consistently show that denser SEI forms at low current density. However, the observations to date are somewhat scattered in

that cells with formation cycles at lower current density do not necessarily show less capacity loss. An investigation of silicon alloying kinetics during lithiation of nano and micro-Si particles ( $D = 50$  nm and  $3\text{--}7$   $\mu\text{m}$ , respectively) reported that a C-rate of 0.1C is slow enough to produce SEI's that are similar in spite of the difference in current density, based on observing similar impedance spectra.<sup>[34]</sup>

In order to evaluate the effect of formation current density on irreversible capacity loss, additional experiments were implemented using the samples with different particle sizes (80 and 500 nm). Unlike the primary experiments reported in Figure 3, all of these experiments used a formation cycle with the same current density per surface area ( $0.58 \mu\text{Ah cm}^{-2}$ ), based on the estimated particle surface area (i.e., such that the 80 and 500 nm particles were subjected to  $\approx C/15$  and  $C/60$  rates, respectively). Subsequent cycles were then run under identical conditions ( $C/20$ ). These additional results provide a direct comparison of initial SEI's formed with the same current density on different sized particles. A larger capacity loss per area with increasing particle size is still observed (see Figure S6 in the Supporting Information), which confirms that our primary conclusions are not significantly altered by variations in the current density during the initial cycle. Thus, while different current densities might produce some differences in the initial SEI structure, these are not substantial enough to change the primary trends observed in Figure 3.

### 2.3. Deformation Model

The  $\Delta\hat{c}$  values in Figure 3 indicate that there is a complex relationship between the overall capacity loss in the electrode and the silicon surface area. Prior studies with graphite electrodes show simpler behavior, where  $\Delta\hat{c}$  does not vary significantly with particle size.<sup>[35,36]</sup> In contrast to this, the results in Figure 3 clearly indicate that  $\Delta\hat{c}$  increases as the Si particle size increases. This unexpected result is likely to be associated with the large volume changes in the silicon electrodes. Although these expansions and contractions occur irrespective of the particle size, the corresponding deformation fields that are produced in the SEI layer can vary with particle size. These effects are addressed with a detailed model. There are a number of existing models for the lithiation of a Si NP, but these have not considered the SEI deformation in detail.<sup>[37–40]</sup>

When a silicon particle is fully lithiated as shown in Figure 4, the expansion produces strains in the SEI that are much larger

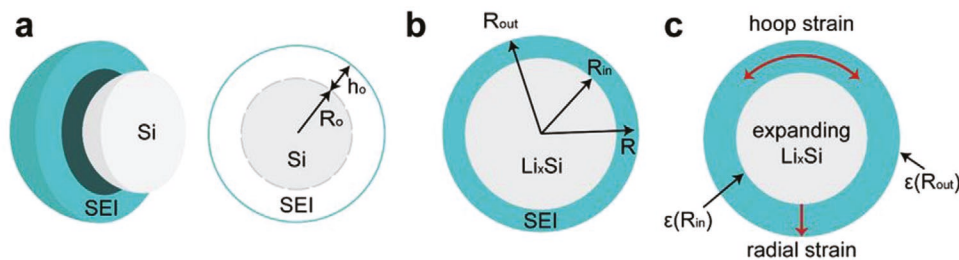


**Figure 4.** Cross-sectional schematics of an expanding silicon particle upon lithiation: a) unlithiated and b) lithiated. c) Schematic of the hoop strain and radial strain in the SEI.

than any reasonable estimate of the elastic limits. Therefore, an appropriate description requires a large deformation model that includes plasticity in the SEI. The analyses of the SEI strain fields presented here assume that the Si particles undergo uniform lithiation. The strict validity of this depends on the particle size, cycling rate, and the Li diffusivity in Si. For the latter, literature values span a wide range, from  $10^{-10}$  to  $10^{-14}$  cm<sup>2</sup> s<sup>-1</sup>.<sup>[41–44]</sup> With a lower limiting value of  $D \approx 10^{-14}$  cm<sup>2</sup> s<sup>-1</sup>, a 20 h lithiation process (i.e., C/20 in the experiments) corresponds to a characteristic diffusion length of

$$L_d = \sqrt{4Dt} \approx 536 \text{ nm} \quad (4)$$

This is larger than the initial radii of the Si NPs used in the experiments (although it is rather close to the lithiated size of the largest particles). Based on this lower bound value of  $L_d$  a uniform Li concentration in the Si NP is a reasonable assumption. With this uniform lithiation the expanding Si NP is subjected to a hydrostatic pressure due to the constraint of the SEI. Here, von Mises yield criterion is adopted, and thus the hydrostatic stress state does not induce plastic deformation in the lithiated Si.

To focus on the SEI at higher state of charge (SOC), a finite deformation model is adopted here to account for the large volume expansion of the particles. SEI growth is neglected for this analysis. This is based on the premise that SEI is largely created during the first cycle, and that changes which occur during subsequent cycles have a limited effect on the SEI deformation occurring during a given cycle. The full model framework treats the SEI as an elastic-perfectly plastic material. These simulations were performed using the commercial software ABAQUS (Dassault Systemes Simulia Corp., Johnston, RI). The Si NP volume change induced by lithiation is determined by the following relationship

$$\Delta v = (V - V_0) / V_0 = 2.7 \times \text{SOC} \quad (5)$$

where the SOC is a fractional value between 0 and 1,  $V$  is volume of lithiated silicon and  $V_0$  is the initial volume.<sup>[3,45]</sup> Logarithmic strain is adopted to model finite deformation. Thus, the increment of lithiation-induced compositional strain due to incremental SOC is given by

$$d\epsilon^c = \frac{0.9}{1 + 2.7 \times \text{SOC}} \times d(\text{SOC}) \quad (6)$$

This is implemented with a user subroutine UEXPAN via a thermal strain analogy. The model parameters employed here are listed in **Table 2**. Varying the SEI modulus between 1 and

**Table 2.** Material properties adopted in the finite element model.

Material Property	Value	Ref.
Li <sub>x</sub> Si Young's modulus [GPa]	40	[65]
Li <sub>x</sub> Si Poisson's ratio	0.26	[65]
SEI Young's modulus [GPa]	5	
SEI Poisson's ratio	0.3	
SEI yield stress [MPa]	10	[51]

5 GPa has a negligible effect on the results since deformation of the SEI is primarily governed by its yield stress (10 MPa). While the model employed here treats the SEI as a continuum with uniform properties, it is important to note that the SEI is composed of multiple phases, and in some cases there is evidence of two layers with different chemical compositions.<sup>[8,46–48]</sup> These variations in the SEI structure can alter the relevant properties. However, to limit the number of unknown parameters, the full SEI heterogeneity was not directly incorporated into the current model. This reflects the current lack of understanding of SEI structure–properties relationships. For example, available data about the SEI modulus show that it depends on electrode materials, electrolyte types, measuring techniques, and locations. However, these studies do not provide specific information about how these variations are related to the SEI composition and nanostructure.<sup>[47,49,50]</sup> Also, there is very little work addressing plastic deformation of SEI, and thus the yield strengths of the organic and inorganic components of SEI are not currently known.<sup>[51,52]</sup>

It is possible to make different assumptions about unknown properties, and evaluate how these affect the results (e.g., in our recent model on mechanical degradation in SEI on Si island electrodes, we studied the effect of different moduli and yield strengths of a bilayer SEI on SEI cracking and delamination).<sup>[53]</sup> However, introducing additional unknown quantities does not greatly affect the results or conclusions in the current study, since the strains in the SEI are largely determined by Si expansion. Thus, we employed a simpler SEI model to interpret the experimental results with a limited number of parameters. More complex SEI behavior that is not yet well understood, such as heterogeneity and chemomechanical interactions, will be integrated into this model when more direct information is available.

The FEM analysis in this study is aligned with the C/20 formation cycle experiments, with an initial SEI thickness of 56 nm that is based on previously reported experimental results that employ the same cycling conditions with continuous films.<sup>[12]</sup> By using unlithiated and stress-free particles as the reference configuration (i.e., zero strain), the model describes tensile hoop strains and compressive radial strains as seen in **Figure 5**.

Large deformation clearly occurs in the SEI during lithium insertion into the Si NPs. **Figure 5a** shows that the maximum tensile hoop strains occur at the boundary between the alloyed particle and the SEI. These hoop strains in the SEI decrease farther from the expanding silicon core. The decreasing SEI thickness with larger particles is due to the combined effects of volume conservation in the SEI and the larger relative expansion of the Si core. For smaller particles relatively low hoop strains occur at the outer part of the SEI. The hoop stress also decreases farther from the Si core as seen in **Figure 5**, and this is less pronounced with smaller particles.

The radial strains and stresses in **Figure 5e,g** are always compressive during lithiation. It can be seen that the radial strain variation across the SEI is larger for smaller particles. This means that the inner part of the soft SEI accommodates a lot of the volume expansion with the smaller particles, such that the outer SEI surface with smaller particles undergoes lower tangential strains. While plasticity dominates the strains, the stresses reflect elastic deformation. The latter were further examined by analyzing the infinitesimal net volume change of the SEI element

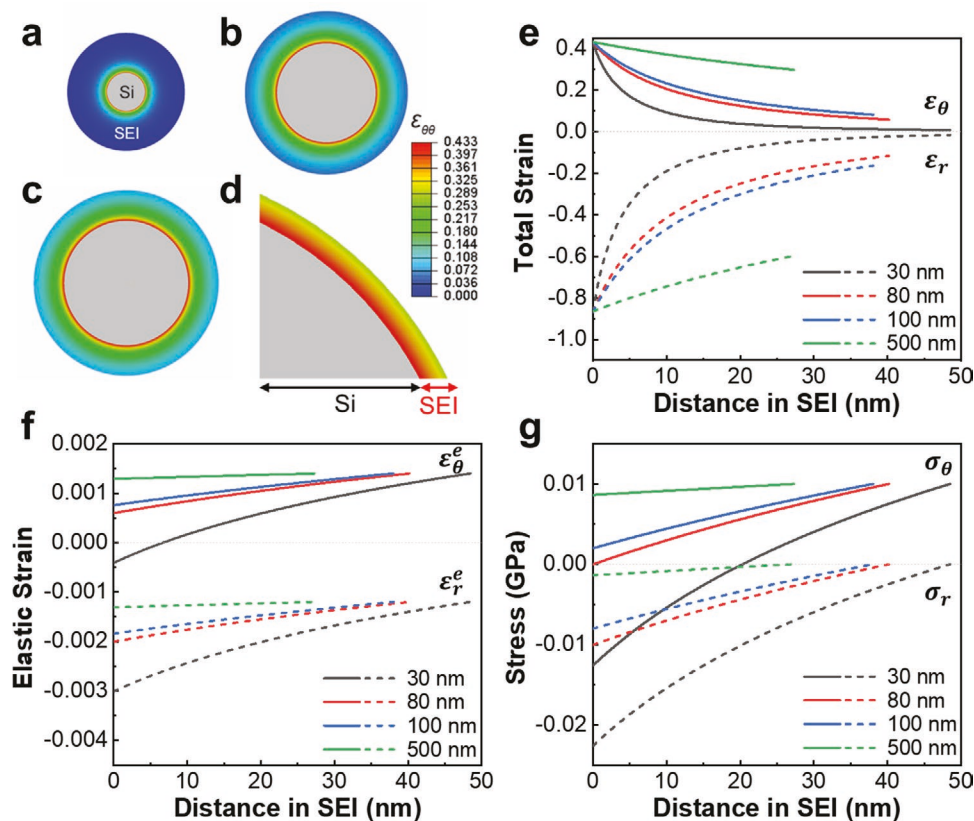


**Figure 5.** Contour plots of the hoop strain in the SEI layer on the a) 30 nm, b) 80 nm, c) 100 nm particle, and d) 500 nm particle (only a portion is shown). e) Total hoop strains and radial strains and f) elastic hoop strains and radial strains in the SEI of Si nanoparticles with different particle sizes calculated with FEM; Larger Si nanoparticles induce higher tensile hoop strain in the SEI. g) Hoop stresses and radial stresses in the SEI of Si nanoparticles with different particle sizes calculated with FEM; Larger Si nanoparticles induce higher tensile hoop stress in the SEI. Solid lines indicate hoop strain/stress and dashed lines indicate radial strain/stress.

at  $R_{in}$ , the particle/SEI interface. The elastic contribution of the strains versus depth into the SEI is extracted from the FEM as seen in Figure 5g. Here, elastic strains vary with particle size at  $R_{in}$  unlike the total strains. The effects of elastic radial and hoop strains can also be combined to obtain the net volume change of the SEI near the interface with the following

$$\Delta V_s = V' - V_o \quad (7)$$

$$V' = V_o (1 + \epsilon_\theta)(1 + \epsilon_r) \approx V_o (1 + 2\epsilon_\theta + \epsilon_r) \quad (8)$$

The value of  $\Delta V_s$  is the net volume change induced by the elastic deformation, in the context of the plastic framework that is adopted here where the plastic deformation in the SEI is assumed to be incompressible.

The plots in Figure 6 are designed to examine correlations between the electrochemical cycling results and the FEM calculations. The capacity loss values for the last symmetric cycles of each sequence (full lithiation followed by full delithiation) are plotted on the vertical axes. The horizontal axes then show predicted deformations at full lithiation, based on the FEM.

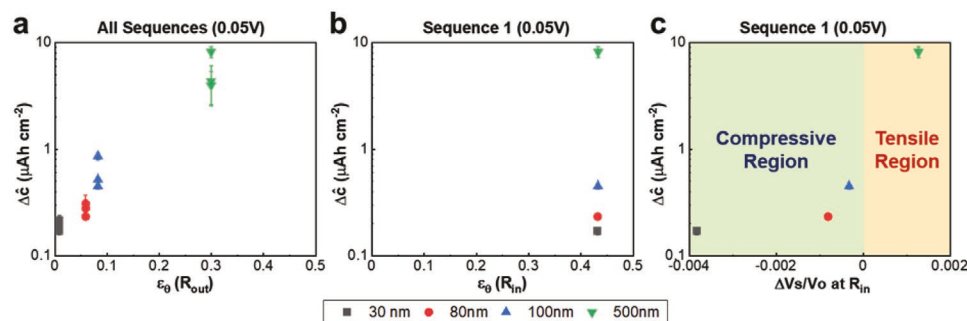


**Figure 6.** Log scale of capacity loss per area (experimental) versus hoop strains (FEM) for Si NPs: a) at  $R_{out}$ , the outer surface of the SEI for all sequences; b) at  $R_{in}$ , the particle/SEI interface. c) Log scale of capacity loss per area versus net volume change at  $R_{in}$ .

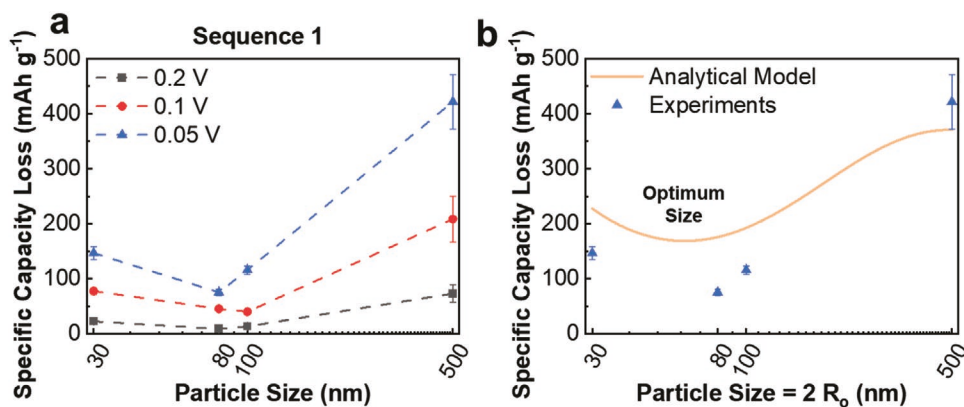


**Figure 7.** a) Specific capacity loss per mass for Sequence 1. b) Specific capacity loss versus particle radius at 0.05 V predicted using Equation (A8).

Figure 6a indicates that higher hoop strains in the SEI occur with larger particles, and these are correlated with higher capacity losses. Figure 6b reflects the fact that the maximum tensile hoop strains occur at the boundary between the alloyed particle and the SEI, however, the results here also show that these do not change significantly with particle size. Thus, this plot shows that there is no correlation between these strains and the measured variations in  $\Delta\hat{c}$ . In contrast Figure 6c shows that the net elastic deformation (i.e.,  $\Delta V_s/V_o$ ) is a function of the particle size, and that this is also correlated with the measured capacity loss. Here, it is particularly interesting that for small particles the SEI volume element is in net compression, while for large particles (i.e., 500 nm) the SEI is subjected to an elastic expansion.

#### 2.4. Strain-Induced Capacity Loss and Optimum Particle Size

Figure 7a shows the specific capacity loss per mass versus particle size for different cut-off voltages. These results demonstrate that the gravimetric losses go through a minimum (in contrast to the trend in Figure 3, where capacity losses are shown on a per area basis). This indicates that there is an optimum particle size with decreasing  $R_o$ , due to the tradeoff between lower strain induced capacity losses and higher specific surface area. The increased surface area is strictly a geometric effect that has led to the common perception that smaller particles will inherently lead to higher capacity loss on a gravimetric basis.<sup>[54–57]</sup> The optimum particle size in Figure 7a contradicts this expectation, and follows directly from the new experiments which show that capacity loss per area increases with particle size (i.e., in Figure 3). These data show that changing the lower voltage cut-off leads to some variation in the optimum size. Possible causes for this include variations in the SEI properties as a function of potential, and the possible effects of residual crystalline silicon in larger particles that does not fully amorphize during initial cycling. A more detailed evaluation of the factors which define the optimum size requires a better understanding of the phenomena which lead to the capacity loss increases in Figure 3. Initial insight into this can be derived from the FEM in Section 2.3, which shows that the deformation field in the SEI varies with particle size. Two trends that were identified here lead to the following hypotheses: 1) higher tensile hoop

strains near the outer surface of larger particles may enhance SEI failure mechanisms, and 2) higher compressive elastic strains near the inner SEI surface of smaller particles may inhibit degradation of the denser, inner SEI. These two effects are shown schematically in Figure 8, and possible mechanisms related to capacity loss are discussed further below.

Several of the results in Figures 5 and 6 show that there is an intriguing correlation between the tensile hoop strains at the outer surface of the SEI and the unexpected observation that specific capacity losses increase with larger particle size. While the FEM does not provide a mechanistic interpretation, it is possible that the higher tensile hoop strains lead to more capacity loss (on a per area basis). This is similar to the strong correlation between in-plane SEI strains and capacity loss that was demonstrated in recent thin film experiments, where we also proposed several possible explanations based on different SEI fracture mechanisms.<sup>[12]</sup> In this previous work, the large in-plane strains that were applied to the SEI lead to large in-plane deformations. There are some similarities between this and the FEM for SEI that is thin relative to the particle size. The thin film limiting case is similar to the calculations which correspond to the 500 nm particles, where the radial principal strains near the outer surface are small and the two principal hoop strains are equal. The deformed state with the same SEI thickness is significantly different for the smaller particles, where the in-plane displacement at the outer surface is nearly zero. In general, when the SEI thickness is similar to or larger than the particle radius, the softer SEI can better accommodate some of the particle expansion via radial deformation. This suggests that with larger particles, the correlation between the higher capacity loss and increased tensile hoop strains at the outer surface, resembles the thin film experiments where large strain-induced capacity losses were also observed. One possibility is that this creates radial cracks in the SEI, as shown in Figure 4c, which have also been directly observed in thin film experiments where it leads to spallation of the SEI.<sup>[7,53]</sup> This can increase capacity loss by exposing new electrode surfaces to the electrolyte, and thus provides one plausible explanation for the results in Figure 6. The lower capacity loss with smaller silicon particles observed here then occurs because the smaller hoop strains at the SEI surface result in less damage. The FEM analysis further confirms that a low  $h_o/R_o$  ratio and large elastic modulus mismatch between the silicon and the softer SEI promotes this effect.

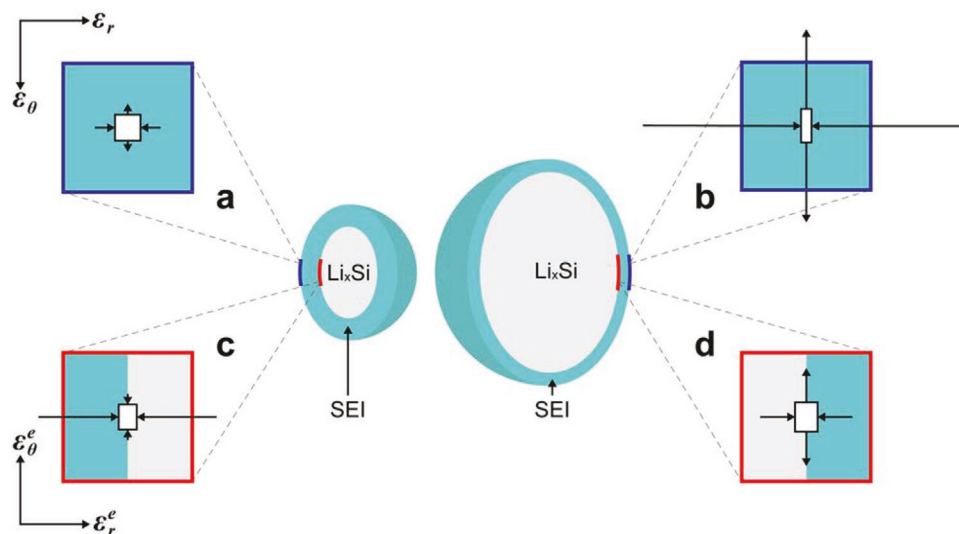


**Figure 8.** Illustration of the infinitesimal volume elements. The lengths of the arrows in the insets reflect the magnitude of the strain. a,b) Total strains near the outer surface. The strains in (a) are much smaller, and thus these arrows are scaled by 5x compared to (b). c,d) Elastic strains near the SEI/particle interface for a small and large particle. Elastic strains in (c) and (d) are scaled to 100x of the total strains.

Another plausible explanation for the lower specific capacity loss with small particles is based on variations in the compressive elastic strain near the inner SEI surface, as shown in Figures 5g and 6c. Here, it is possible that the net compression near the inner SEI surface in Figure 6c inhibits transport through a mesoporous SEI structure and thus improves passivation. The degradation of the inner SEI may also be inhibited by the net compression that occurs with smaller particles. These mechanisms are potentially complex, but one possibility is that the inner compressive stress improves adhesion to the underlying silicon particle when it shrinks back during delithiation (i.e., because the elastic restoring force in this compressed SEI will be applied toward the center of the particle).

The effects that are outlined above demonstrate two different ways in which the particle size alters the deformation field in the SEI. In principle, either of these can account for the optimum particle size observed in Figure 7. Basic models that capture these effects can be constructed, but they necessarily rely on a relationship between the SEI stress state and excess capacity loss. These can be constructed empirically from the relationships that are shown in the data that is plotted in Figure 6. As one example, consider a simple description which assumes that the specific capacity loss is given by

$$\Delta\hat{c} \cong \Delta\hat{c}_0 + \Delta\hat{c}_{\text{out}}^S \Delta\alpha_{\text{out}} \quad (9)$$

where  $\Delta\hat{c}_0$  is the capacity loss occurring in the absence of any applied strains and  $\Delta\hat{c}_{\text{out}}^S$  describes excess loss that is proportional to the increased strain at the outer SEI surface. The relative area increase at this position after lithiation,  $\Delta\alpha_{\text{out}}$ , provides an estimate of the hoop strains and is given by

$$\Delta\alpha_{\text{out}} = \left[ 1 + \frac{\Delta v}{(1 + \psi_0)^3} \right]^{2/3} - 1 \quad (10)$$

where and  $\psi_0 = h_0/R_0$ . This model, presented in more detail in the Appendix, can be fit to the experimental data, as shown in Figure 7b. The optimum particle size observed in the experiments is properly described by this model, but a more detailed description of  $\Delta\hat{c}$  is apparently needed to provide better quantitative accuracy. This can be accomplished empirically by extending Equation (10) (for example, if  $\Delta\hat{c}$  is a stronger function of  $\Delta\alpha_{\text{out}}$ ). Alternative models based on the stress state at the inner SEI/electrode interface can also be created. However, these more detailed formulations should be based on more precise experiments (otherwise, using these approaches to improve the fit in Figure 7b merely corresponds to curve fitting with more parameters). In the absence of this information, the simple model based on Equation (9) is still useful as a demonstration that the optimum particle size observed in the experiments can be properly described as a tradeoff between the increase in specific surface area that occurs as particle size decreases, and the increase in strain induced capacity loss that occurs as particle size increases.

### 3. Conclusion

The research presented here evaluates the impact of SEI strains on irreversible capacity losses by investigating composite electrodes with different Si particle sizes. The results show lower specific capacity loss (normalized to the initial area) with smaller particles. To explain this finding, FEM was employed to describe the strains in the SEI as a function of particle size. This analysis incorporates both large deformations and plasticity effects, based on the idea that the mismatch of elastic modulus between relatively soft SEI and the stiffer silicon core will affect the strain-states in the SEI. The model points to at least two possible explanations for the decrease in specific capacity loss that occurs as the particle size decreases: 1) the tensile hoop strains in the outer portion of the SEI decrease,

and 2) the overall elastic strains in the inner portion become more compressive. Both of these results indicate that with smaller particles, the relatively soft SEI is better able to accommodate the large radial deformations that occur during the lithiation of the silicon particles.

While the higher specific surface areas of smaller particles will increase initial SEI formation, our results also demonstrate that smaller particles lead to SEI deformation, as the SEI is more resistant to mechanical degradation. The combination of these effects is consistent with the optimum particle size observed in the experiments, where capacity loss per volume is minimized. This result has important ramifications, primarily because it indicates that the advantages of using smaller silicon particles (faster lithiation, reduced particle fracture, etc.) will not necessarily be accompanied by higher capacity losses due to SEI formation. Our results also indicate that capacity loss is strongly influenced by the SEI deformation around Si particles. The control of this behavior will ultimately depend on a variety of the chemomechanical properties of the SEI.

#### 4. Experimental Section

**Electrode Preparation:** Four different sizes of silicon nanoparticles (Si NPs, average particle size 20–30 nm, 99% purity, specific surface area 80–150 m<sup>2</sup> g<sup>-1</sup>, US Research Nanomaterials Inc., 80 nm, 99% purity, specific surface area 45 m<sup>2</sup> g<sup>-1</sup> US Research Nanomaterials Inc., 100 nm (BET), <3% oxygen passivation, Sigma-Aldrich, and 500 nm, 99% purity, D50 = 500 nm, US Research Nanomaterials Inc.) were used as active materials in the composite electrodes. Super P carbon black (Timcal) was used as a conductive additive and Carboxymethyl Cellulose (CMC, Sigma-Aldrich) as binder. The formation cycle of the carbon black has limited reversible capacity (≈200 mAh g<sup>-1</sup>), which is far lower than that of the silicon nanoparticles.<sup>[58]</sup>

The slurry was prepared with Si NPs, carbon black and binder loadings of 70, 15, and 15 weight percent (wt%), respectively. Each slurry contained either the 30, 80, 100, or 500 nm sized Si NPs. By limiting the Si loading to 70 wt%, the electrodes exhibit better reversible cycling than comparable electrodes with more Si. CMC was dissolved in distilled water to obtain a 5 wt% CMC binder solution. Si NPs and carbon black powders were first dry-mixed using a mortar and a pestle. Then the binder solution was added into the mortar and mixed further. Additional distilled water was introduced (≈1 mL) to optimize the viscosity of the slurry for adequate coating. The slurry was then transferred into a small beaker (10 mL) and homogenized further using a homogenizer (Bio-Gen PRO200, PRO Scientific) at 500 rpm for 60 min.

The slurry was coated onto a 25 μm thick copper foil using a doctor blade. The blade clearance was set to 150 μm for thickness adjustment. The coated foil was first air-dried inside the fume hood at room temperature for an hour and dried further in a vacuum oven at 75 °C overnight to fully evaporate the remaining solvent of the electrode. For coin cell assembly, 12.5 mm electrode disks were cut and the loading of the active materials was about 1 mg cm<sup>-2</sup>. Electrode thicknesses of 35–45 μm (including the copper substrate) were measured with a digital micrometer (Mitutoyo) before cycling.

**Electrochemical Cycling:** The composite electrodes described in the electrode preparation section was placed and assembled in CR-2032 coin cells inside an argon-filled glove box. The prepared electrodes were used as working electrodes and Li foil was used as both the counter and reference electrode. The electrolyte was a mixed solution of 1 M LiPF<sub>6</sub> in ethylene carbonate and ethyl methyl carbonate (3:7 volume ratio, Gotion, USA). Galvanostatic discharge/charge tests were performed in the voltage window of 0.05–1.5 V (vs Li<sup>+</sup>/Li) with a Bio-Logic VMP-3 potentiostat.

**Characterization of Material Properties:** The morphology and particle size of the electrode samples were characterized using a HR-TEM, JEOL

2100F and a SEM (FEI HELIOS 600). Si NP powders were characterized using an X-ray photoelectron spectrometer (K-Alpha, Thermo Scientific) to obtain native oxide information. An X-ray diffractometer (Bruker D8 Discover) was used to obtain diffraction patterns of the pristine powder, electrode as-made, after formation cycle, and after sequence 1. Cycled coin cells were disassembled inside the glove box, and the electrodes were rinsed with dimethyl carbonate to remove electrolyte residue and dried in Ar atmosphere.

#### Appendix

To provide further insight into the comparisons in Figure 6, note that the hoop strains at  $R_{in}$  and  $R_{out}$  are closely related to the area changes at these two positions. These are readily evaluated for an idealized spherical particle, where the volume change for an arbitrary SOC is given by

$$\Delta v \equiv \frac{R_{in}^3 - R_o^3}{R_o^3} \quad (A1)$$

where  $R_{in}$  is the radius of the lithiated particle. The relative change in the area of the particle/SEI interface is then

$$\Delta \alpha_{in} = \frac{R_{in}^2 - R_o^2}{R_o^2} = (1 + \Delta v)^{2/3} - 1 \quad (A2)$$

where Equation (5) gives the relationship between  $\Delta v$  and the SOC. This illustrates that  $\Delta \alpha_{in}$  is independent of  $R_o$ , which is consistent with the Figure 6a FEM results showing that the initial particle size does not significantly impact the hoop strains at  $R_{in}$ .

An estimate of  $R_{out}$  is then based on a fixed SEI volume (after the formation cycle), with the assumption that plastic flow of the SEI creates a conformal film on the expanding particle. This leads to

$$(R_{in} + h)^3 - R_{in}^3 = (R_o + h_o)^3 - R_o^3 \quad (A3)$$

where  $h$  is the SEI thickness. This gives

$$\Delta \alpha_{out} = \frac{R_{out}^2 - (R_o + h_o)^2}{(R_o + h_o)^2} = \frac{(R_{in} + h)^2 - (R_o + h_o)^2}{(R_o + h_o)^2} \quad (A4)$$

where  $R_{out} = R_{in} + h$ . Equations (A3) and (A4) can then be solved to obtain  $h$  and  $\Delta \alpha_{out}$  for a given SOC, which leads to

$$\Delta \alpha_{out} = \left[ 1 + \frac{\Delta v}{(1 + \psi_o)^3} \right]^{2/3} - 1 \quad (A5)$$

where  $\psi_o = h_o/R_o$ . The variation of  $\Delta \alpha_{out}$  with  $R_o$  in this expression can be used to track the hoop strains at the outer surface,  $\epsilon_{\theta\theta}(R_{out})$ , that were obtained from the FEM. To permit further analysis of the data, the relationship between  $\Delta \hat{c}$  and  $R_o$  observed in the experiments (i.e., in Figure 3) was then described with

$$\Delta \hat{c} \equiv \Delta \hat{c}_o + \Delta \hat{c}_{out}^S \Delta \alpha_{out} \quad (A6)$$

where  $\Delta \hat{c}_o$  is the specific capacity loss in the absence of any applied strains, and  $\Delta \hat{c}_{out}^S$  describes the strain-induced capacity loss. This approximate expression is based on the correlation between  $\Delta \hat{c}$  and  $\epsilon_{\theta\theta}(R_{out})$  (i.e., in Figure 6b,c). Combining this with Equation (A5) gives

$$\Delta \hat{c} = \Delta \hat{c}_o + \Delta \hat{c}_{out}^S \left( \left[ 1 + \frac{\Delta v}{(1 + \psi_o)^3} \right]^{2/3} - 1 \right) \quad (A7)$$

where the impact that particle size has on capacity losses is described with only  $\psi_o$ . With this relationship, the size effect disappears at sufficiently large  $R_o$  (i.e., where  $\Delta \alpha_{out} \rightarrow \Delta \alpha_{in}$  as  $\psi_o \rightarrow 0$ ). To obtain an

approximate description of the experimental results, data for different sequences and cutoff voltages were fit with Equation (A7) to obtain values for  $\Delta\hat{c}_o$  and  $\Delta\hat{c}_{out}^S$ . The examples in Figure S7 (Supporting Information) demonstrate that this approach provides a reasonable description of the experimental results.

The idea of an optimum particle size can be conveniently demonstrated by employing Equation (A7). For a spherical particle, combining Equations (2), (3), and (A7) gives a description of  $\Delta c$  ( $R_o$ )

$$\Delta c = \frac{3}{\rho R_o} \left[ \Delta\hat{c}_o + \Delta\hat{c}_{out}^S \left( \left[ 1 + \frac{\Delta v R_o^3}{(R_o + h_o)^3} \right]^{\frac{2}{3}} - 1 \right) \right] \quad (\text{A8})$$

For a given SOC and  $h_o$ , the value of  $R_o^{\text{OPT}}$  (optimum particle size) can be estimated by setting the derivative of Equation (A8) to zero. The  $\Delta c$  values plotted in Figure 7b show that Equation (A8) predicts an optimum particle size. Reported SEI thicknesses on Si electrodes vary over a wide range from roughly ten to several hundred nanometers.<sup>[7,45–47,59–64]</sup> The results in Figure 7b show that an approximate value of 100 nm leads to rough agreement between Equation (A8) and with the trends observed in our experiments. There are discrepancies between this model and the data, largely because the formulation in Equations (A6)–(A8) is relatively simple. This suggests that more accurate predictions require a more detailed model. One possible improvement is that  $\Delta\hat{c}_{out}^S$  probably increases with the strain (i.e.,  $\Delta\hat{c}_{out}^S$  is not constant, but is instead an increasing function of  $\Delta\alpha_{out}$ ). A phenomenological description that incorporates this effect with an additional parameter improves the fit in Figure S7 (Supporting Information). However, the simpler form in Equation (A8) illustrates that the size ratio  $\psi_o$  is an important quantity that reflects the strain distribution in the SEI, and is directly correlated with capacity loss. This also indicates that the SEI thickness has a significant impact on the optimum particle size.

For comparison, note that the minimum observed in Figure 7b is not observed with graphite electrodes. This is consistent with the simple model used to obtain the fit here. For a limiting case where there is no volume change in the active material,  $\Delta v = 0$  in Equation (10) and  $\Delta c$  is inversely proportional to  $R_o$ . For graphite,  $\Delta v$  is nonzero but it is substantially smaller than it is for Si. Thus, for graphite the 2nd term on the rhs of Equation (9) is still relatively small. This is consistent with experiments which show that SEI losses for graphite electrodes decrease monotonically with increasing particle size, without the minimum seen in Figure 7b.

## Supporting Information

Supporting Information is available from the Wiley Online Library or from the author.

## Acknowledgements

The authors acknowledge research support from General Motors, the National Science Foundation (DMR-1832829) and SK Innovation.

## Conflict of Interest

The authors declare no conflict of interest.

## Data Availability Statement

Research data are not shared.

## Keywords

anode materials, lithium-ion batteries, silicon nanoparticles, solid electrolyte interphase, strain-induced capacity loss

Received: December 11, 2020

Revised: January 21, 2021

Published online: February 28, 2021

- [1] A. N. Dey, *J. Electrochem. Soc.* **1971**, *118*, 1547.
- [2] D. Larcher, S. Beattie, M. Morcrette, K. Edström, J. C. Jumas, J. M. Tarascon, *J. Mater. Chem.* **2007**, *17*, 3759.
- [3] L. Y. Beaulieu, T. D. Hatchard, A. Bonakdarpour, M. D. Fleischauer, J. R. Dahn, *J. Electrochem. Soc.* **2003**, *150*, A1457.
- [4] M. T. McDowell, S. W. Lee, W. D. Nix, Y. Cui, *Adv. Mater.* **2013**, *25*, 4966.
- [5] J. L. Goldman, B. R. Long, A. A. Gewirth, R. G. Nuzzo, *Adv. Funct. Mater.* **2011**, *21*, 2412.
- [6] E. Peled, *J. Electrochem. Soc.* **1997**, *144*, L208.
- [7] R. Kumar, A. Tokranov, B. W. Sheldon, X. Xiao, Z. Huang, C. Li, T. Mueller, *ACS Energy Lett.* **2016**, *1*, 689.
- [8] A. Tokranov, R. Kumar, C. Li, S. Minne, X. Xiao, B. W. Sheldon, *Adv. Energy Mater.* **2016**, *6*, 1502302.
- [9] Z. L. Xu, K. Lim, K. Y. Park, G. Yoon, W. M. Seong, K. Kang, *Adv. Funct. Mater.* **2018**, *28*, 1.
- [10] U. Kasavajula, C. Wang, A. J. Appleby, *J. Power Sources* **2007**, *163*, 1003.
- [11] P. Verma, P. Maire, P. Novák, *Electrochim. Acta* **2010**, *55*, 6332.
- [12] W. Zhang, T. H. Cai, B. W. Sheldon, *Adv. Energy Mater.* **2019**, *9*, 1.
- [13] C. K. Chan, H. Peng, G. Liu, K. McIlwrath, X. F. Zhang, R. A. Huggins, Y. Cui, *Nat. Nanotechnol.* **2008**, *3*, 31.
- [14] J. Graetz, C. C. Ahn, R. Yazami, B. Fultz, *Electrochem. Solid-State Lett.* **2003**, *6*, A194.
- [15] R. Fong, U. von Sacken, J. R. Dahn, *J. Electrochem. Soc.* **1990**, *137*, 2009.
- [16] C. K. Chan, R. Ruffo, S. S. Hong, Y. Cui, *J. Power Sources* **2009**, *189*, 1132.
- [17] H. Wu, G. Chan, J. W. Choi, I. Ryu, Y. Yao, M. T. McDowell, S. W. Lee, A. Jackson, Y. Yang, L. Hu, Y. Cui, *Nat. Nanotechnol.* **2012**, *7*, 310.
- [18] L. Zhang, Y. Liu, B. Key, S. E. Trask, Z. Yang, W. Lu, *ACS Appl. Mater. Interfaces* **2017**, *9*, 32727.
- [19] Y. Oumellal, N. Delpuech, D. Mazouzi, N. Dupré, J. Gaubicher, P. Moreau, P. Soudan, B. Lestriez, D. Guyomard, *J. Mater. Chem.* **2011**, *21*, 6201.
- [20] M. Tokur, M. Y. Jin, B. W. Sheldon, H. Akbulut, *ACS Appl. Mater. Interfaces* **2020**, *12*, 33855.
- [21] N. Wan, X. Lu, Y. Wang, W. Zhang, Y. Bai, Y. S. Hu, S. Dai, *Sci. Rep.* **2016**, *6*, 1.
- [22] F. Zhang, G. Zhu, K. Wang, X. Qian, Y. Zhao, W. Luo, J. Yang, *J. Mater. Chem. A* **2019**, *7*, 17426.
- [23] C. Xiao, P. He, J. Ren, M. Yue, Y. Huang, X. He, *RSC Adv.* **2018**, *8*, 27580.
- [24] A. R. Kamali, H. K. Kim, K. B. Kim, R. Vasant Kumar, D. J. Fray, *J. Mater. Chem. A* **2017**, *5*, 19126.
- [25] T. Jaumann, J. Balach, M. Klose, S. Oswald, U. Langklotz, A. Michaelis, J. Eckert, L. Giebeler, *Phys. Chem. Chem. Phys.* **2015**, *17*, 24956.
- [26] A. Casimir, H. Zhang, O. Ogoko, J. C. Amine, J. Lu, G. Wu, *Nano Energy* **2016**, *27*, 359.
- [27] M. T. McDowell, I. Ryu, S. W. Lee, C. Wang, W. D. Nix, Y. Cui, *Adv. Mater.* **2012**, *24*, 6034.
- [28] X. H. Liu, L. Zhong, S. Huang, S. X. Mao, T. Zhu, J. Y. Huang, *ACS Nano* **2012**, *6*, 1522.

- [29] T. Zhu, Q. Hu, G. Yan, J. Wang, Z. Wang, H. Guo, X. Li, W. Peng, *Energy Technol.* **2019**, *7*, 1.
- [30] S. S. Zhang, K. Xu, T. R. Jow, *J. Power Sources* **2004**, *130*, 281.
- [31] S. Kranz, T. Kranz, T. Graubner, Y. Yusim, L. Hellweg, B. Roling, *Batter. Supercaps* **2019**, *2*, 1026.
- [32] Y. Rangom, R. R. Gaddam, T. T. Duignan, X. S. Zhao, *ACS Appl. Mater. Interfaces* **2019**, *11*, 34796.
- [33] Y. He, M. Liu, Z. Huang, B. Zhang, Y. Yu, B. Li, F. Kang, J.-K. Kim, *J. Power Sources* **2013**, *239*, 269.
- [34] Y. Ko, C. Hwang, H. K. Song, *J. Power Sources* **2016**, *315*, 145.
- [35] H. Wang, T. Ikeda, K. Fukuda, M. Yoshio, *J. Power Sources* **1999**, *83*, 141.
- [36] L. S. Roselin, R.-S. Juang, C.-T. Hsieh, S. Sagadevan, A. Umar, R. Selvin, H. H. Hegazy, *Materials* **2019**, *12*, 1229.
- [37] K. Zhao, M. Pharr, S. Cai, J. J. Vlassak, Z. Suo, *J. Am. Ceram. Soc.* **2011**, *94*, s226.
- [38] K. Zhao, M. Pharr, Q. Wan, W. L. Wang, E. Kaxiras, J. J. Vlassak, Z. Suo, *J. Electrochem. Soc.* **2012**, *159*, A238.
- [39] Z. Cui, F. Gao, J. Qu, *J. Mech. Phys. Solids* **2012**, *60*, 1280.
- [40] Z. Cui, F. Gao, J. Qu, *J. Mech. Phys. Solids* **2013**, *61*, 293.
- [41] T. L. Kulova, Y. V. Pleskov, A. M. Skundin, E. I. Terukov, O. I. Kon'kov, *Russ. J. Electrochem.* **2006**, *42*, 708.
- [42] N. Ding, J. Xu, Y. X. Yao, G. Wegner, X. Fang, C. H. Chen, I. Lieberwirth, *Solid State Ionics* **2009**, *180*, 222.
- [43] R. Ruffo, S. S. Hong, C. K. Chan, R. A. Huggins, Y. Cui, *J. Phys. Chem. C* **2009**, *113*, 11390.
- [44] J. Xie, N. Imanishi, T. Zhang, A. Hirano, Y. Takeda, O. Yamamoto, *Mater. Chem. Phys.* **2010**, *120*, 421.
- [45] I. Yoon, D. P. Abraham, B. L. Lucht, A. F. Bower, P. R. Guduru, *Adv. Energy Mater.* **2016**, *6*, 1600099.
- [46] A. Tokranov, B. W. Sheldon, C. Li, S. Minne, X. Xiao, *ACS Appl. Mater. Interfaces* **2014**, *6*, 6672.
- [47] J. Zheng, H. Zheng, R. Wang, L. Ben, W. Lu, L. Chen, L. Chen, H. Li, *Phys. Chem. Chem. Phys.* **2014**, *16*, 13229.
- [48] J. Nanda, G. Yang, T. Hou, D. N. Voylov, X. Li, R. E. Ruther, M. Naguib, K. Persson, G. M. Veith, A. P. Sokolov, *Joule* **2019**, *3*, 2001.
- [49] J. Zhang, R. Wang, X. Yang, W. Lu, X. Wu, X. Wang, H. Li, L. Chen, *Nano Lett.* **2012**, *12*, 2153.
- [50] H. Shin, J. Park, S. Han, A. M. Sastry, W. Lu, *J. Power Sources* **2015**, *277*, 169.
- [51] I. Yoon, S. Jurng, D. P. Abraham, B. L. Lucht, P. R. Guduru, *Energy Storage Mater.* **2020**, *25*, 296.
- [52] Y. Kamikawa, K. Amezawa, K. Terada, *J. Phys. Chem. C* **2020**, *124*, 22488.
- [53] K. Guo, R. Kumar, X. Xiao, B. W. Sheldon, H. Gao, *Nano Energy* **2020**, *68*, 104257.
- [54] V. L. Chevrier, L. Liu, D. B. Le, J. Lund, B. Molla, K. Reimer, L. J. Krause, L. D. Jensen, E. Figgemeier, K. W. Eberman, *J. Electrochem. Soc.* **2014**, *161*, A783.
- [55] M.-T. F. Rodrigues, J. A. Gilbert, K. Kalaga, D. P. Abraham, *J. Phys. Energy* **2020**, *2*, 024002.
- [56] M. Wetjen, D. Pritzl, R. Jung, S. Solchenbach, R. Ghadimi, H. A. Gasteiger, *J. Electrochem. Soc.* **2017**, *164*, A2840.
- [57] P.-K. Lee, Y. Li, D. Y. W. Yu, *J. Electrochem. Soc.* **2017**, *164*, A6206.
- [58] R. Kumar, J. H. Woo, X. Xiao, B. W. Sheldon, *J. Electrochem. Soc.* **2017**, *164*, A3750.
- [59] F. Kong, R. Kostecki, G. Nadeau, X. Song, K. Zaghib, K. Kinoshita, F. McLarnon, *J. Power Sources* **2001**, *97–98*, 58.
- [60] E. Peled, F. Patolsky, D. Golodnitsky, K. Freedman, G. Davidi, D. Schneier, *Nano Lett.* **2015**, *15*, 3907.
- [61] W. Huang, J. Wang, M. R. Braun, Z. Zhang, Y. Li, D. T. Boyle, P. C. McIntyre, Y. Cui, *Matter* **2019**, *1*, 1232.
- [62] J. T. Lee, N. Nitta, J. Benson, A. Magasinski, T. F. Fuller, G. Yushin, *Carbon* **2013**, *52*, 388.
- [63] F. Luo, G. Chu, X. Xia, B. Liu, J. Zheng, J. Li, H. Li, C. Gu, L. Chen, *Nanoscale* **2015**, *7*, 7651.
- [64] I. Yoon, S. Jurng, D. P. Abraham, B. L. Lucht, P. R. Guduru, *Nano Lett.* **2018**, *18*, 5752.
- [65] V. B. Shenoy, P. Johari, Y. Qi, *J. Power Sources* **2010**, *195*, 6825.